

A computational study of structural, electronic and carrier mobility of boron and phosphorus/nitrogen co-doped graphene

Vivek K. Yadav^a, Showkat H. Mir^b, Jayant K. Singh^{a,*}

^a Department of Chemical Engineering, IIT Kanpur, Kanpur, 208016, India

^b Department of Chemistry, IIT Kanpur, Kanpur, 208016, India

ARTICLE INFO

Keywords:

Bandgap
Graphene
Carrier mobility
DFT

ABSTRACT

Opening a bandgap in graphene by doping with lighter elements plays a vital role in the next generation nano-electronic devices. Here, we present the structural, electronic, and mobility of graphene co-doped with boron/nitrogen (BCN) and boron/phosphorus (BCP) using density functional theory with the inclusion of van der Waals interactions. By analyzing the band structure, it is found that BCP shows a direct bandgap whereas BCN exhibits an indirect bandgap. The bandgap values calculated using PBE (HSE) functional are (1.97 eV) (3.19 eV) for BCN and 0.55 eV (1.18 eV) for BCP. From phonon dispersion results, it is apparent that both BCN and BCP shows positive frequencies within the Brillouin zone demonstrating the lattice dynamical stability of these materials. Deformation potential theory is applied to calculate the electron/hole mobility by applying the uniaxial strain along x- and y-directions. It is seen that BCP possess significantly larger mobility compared to BCN. For BCP, the mobility of electron is 1588 (2999) and that of the hole is 1607 (838) along x-direction (y-direction) in units of $\text{cm}^2\text{V}^{-1}\text{s}^{-1}$, respectively, which are larger than MoS_2 . Also, Boltzmann theory within the constant relaxation time approximation is used to determine the temperature dependent conductivity, and the results are consistent with the deformation theory.

1. Introduction

Metal-free semiconductors with narrow bandgap attracted huge attention in the last few decades as they display tremendous electronic applications in infrared devices, Light emitting diodes, electro-catalysts, thermo-photovoltaics, etc. [1–5]. Since the discovery of graphene with massless Dirac fermions [6], many other 2D materials have shown unusual high carrier mobility compared to their bulk counter parts [7]. It was reported that graphene has ultrahigh carrier mobility of $1\text{--}4 \times 10^5 \text{ cm}^2\text{V}^{-1}\text{s}^{-1}$ [8]. But, graphene is a zero bandgap material, therefore doping by hetero-atoms like boron, nitrogen or phosphorus in graphene produces a new class of materials with a finite bandgap and mobility comparable to graphene. The 2D materials created directly from graphene by doping it with lighter elements such as boron, nitrogen and phosphorus have gained much attention due to their electronic and opto-electronic application [9]. The correct choice of foreign elements in graphene to maintain carbon to doping element ratio for generating new 2D materials plays a key role in tailoring its electronic properties and subsequently enhance its device applications [10]. These doped materials display higher mobility ($> 10^3 \text{ cm}^2\text{V}^{-1}\text{s}^{-1}$) compared to other 2D materials such as transition metal chalcogenides, e.g. MoS_2

having carrier mobility $\sim 10^2 \text{ cm}^2\text{V}^{-1}\text{s}^{-1}$ [11–14]. Many attempts have been made to fabricate graphene based devices by tailoring its bandgap via doping [15]. It was reported that Dirac point in the graphene shifts below and above the Fermi level when doped with nitrogen (electron doping) and boron (hole doping). Also, upon co-doping graphene by boron and nitrogen, an energy gap between valence and conduction band appeared about Fermi level, leaving the system with narrow bandgap semiconductor. Besides, it is found that nitrogen doped graphene compound showed bandgap in the range of 1.6–2.0 eV depending upon the nitrogen to carbon ratio, which makes it plausible material for device applications [15]. Similar behavior were also seen by doping graphene with other elements [16–21]. Another promising way is to employ graphene nano ribbons and also tailor their bandgap via lighter element doping. Significant progress was made to develop nitrogen- [22], boron- [23] and phosphorus-doped graphene nanoribbons [24]. In fact, phosphorus doped graphene nanoribbon were found to exhibit a bipolar character [24–26]. It was reported that the p-type boron edge-doped graphene nanoribbon can be converted into an n-type upon introducing a bipolar phosphorus co-dopant atom, forming a B–P complex [24]. In our previous work, we showed that bandgap of boron and nitrogen co-doped graphene is a function of boron-nitrogen

* Corresponding author.

E-mail addresses: viveky@iitk.ac.in (V.K. Yadav), showkath@iitk.ac.in (S.H. Mir), jayantks@iitk.ac.in (J.K. Singh).

pairs and well as their relative position [27]. We also demonstrated that these materials are potential candidates for hydrogen evolution reaction [27] and biological applications [28]. Thus we note that several studies were performed to study the electronic structure of doped graphene, however, the carrier mobility and lattice dynamic stability were not much investigated. Therefore, in present work, our goal is to examine the dynamic stability of lighter non-metal (boron, nitrogen and phosphorus) doped graphene. In addition, we report the carrier mobility of these materials using deformation potential theory, which is an essential property of a material to be used in device applications. Our results has shown that BCP is a potential candidate for future electronic applications as it exhibits a direct bandgap (1.18 eV) and high carrier mobility.

2. Methodology

In this work, first principle calculations were carried out using QUANTUM ESPRESSO [29] package within the framework density functional theory (DFT). The electron-ion interaction was described using Perdew-Burke-Ernzerhof [30] functional with in the framework of generalized gradient approximation (GGA) [31]. To obtain the optimized structural boron-carbon-X systems, the Kohn-Sham wavefunctions were expanded by a plane wave basis set with a kinetic energy cut-off of 50 Ry for electron density and 500 Ry for charge density. Brillouin zone (BZ) integration was done using a uniform Monkhorst-Pack [32] k-point grid of $15 \times 15 \times 1$ for geometry optimization and $50 \times 50 \times 1$ for electronic structure calculations. The atomic positions and cell parameters were fully relaxed in both cases until an energy convergence of 10^{-8} eV reached. Van der Waals interactions were included using DFT-D3 dispersion corrections [33]. As PBE underestimates the bandgap values, therefore, HSE functional [34] was additionally used to compute the bandgap with k-points $10 \times 10 \times 1$. In our calculations, we used a unit cell designed in such a way to have 50% Carbon, 25% boron and remaining 25% nitrogen (phosphorus) atoms. To avoid the interaction between periodic images a large vacuum of 20 Å was employed in the z-direction perpendicular to the sheet. Phonon dispersion of BCN and BCP were obtained employing density functional perturbation theory (DFPT) [35] in the linear response approach using q-points $3 \times 3 \times 1$. This method avoids using supercell approach and allows the calculation of dynamical matrix at arbitrary q-points.

3. Results and discussion

3.1. Structural properties

The optimized structure of BCX (X = nitrogen, phosphorus, hereafter, BCN and BCP respectively) are shown in Fig. 1(a and b). Both cell parameters and atomic positions were allowed to relax during optimization. The calculated lattice parameters **a** and **b** of BCN (BCP) were 4.99 Å (5.65 Å) and 4.35 Å (4.95 Å). Bond lengths C–C, C–N/P, C–B/P and B–N/P calculated for BCN (BCP) were 1.38 (1.42), 1.44 (1.73), 1.47 (1.87) and 1.48 (1.56), respectively. From the calculated bond lengths, it is apparent that BCP show larger lattice parameters and bond lengths due to the bigger atomic size of phosphorus. The structural stability of BCN and BCP nanosheets were also assessed by calculating their cohesive energy (E_{coh}) using equation 1

$$E_{coh} = [E_{tot} - \sum_i n_i E_i] / n \quad (i=C, B, N) \quad (1)$$

where, in the equation, E_{tot} denotes the total energy of BCN or BCP, E_i represents the gas phase atomic energies of B, C and N (P) and n represents the total number of atoms in the sheet. The calculated cohesive energies of BCN and BCP were -8.19 eV and -7.17 eV. This shows that BCN is relatively more stable than BCP. Further, to evaluate the lattice dynamical stability of these nanosheets, the phonon dispersion of

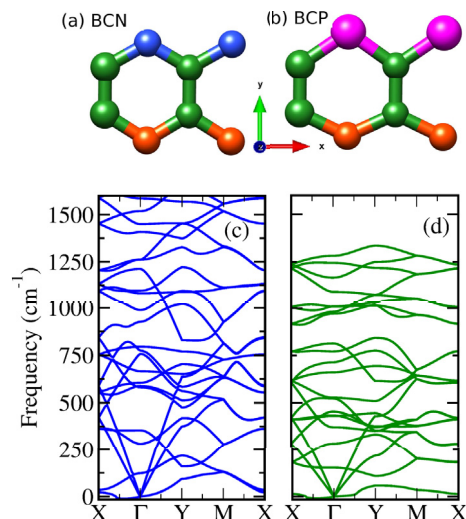


Fig. 1. (a,b) shows the unit cells and (c,d) the phonon dispersion of BCN and BCP, respectively. Here, orange, forest green, blue and pink balls represent the boron, carbon, nitrogen and phosphorus atoms. (For interpretation of the references to colour in this figure legend, the reader is referred to the Web version of this article.)

both BCN and BCP were calculated as shown in Fig. 1(c and d). It is evident from Fig. 1(c and d) that BCN and BCP show dynamical stability as both structures has positive frequency throughout the Brillouin zone. From phonon dispersion plot, it is revealed that the acoustic modes of both materials display large dispersion (~ 600 cm^{-1} in BCN and ~ 500 cm^{-1} in BCP) and cross the optical modes along Γ -X and Γ -Y directions. It is also interesting to see that BCN has maximum frequency value of 1600 cm^{-1} whereas BCP has only 1300 cm^{-1} . This also indicates that BCN possess strong bonds as compared to that of BCP. The maximum frequency mode of BCN is also comparable to that of graphene which exhibits the maximum frequency of 1590 cm^{-1} at Γ -point [36]. Moreover, it is evident from phonon dispersion that atoms move more freely in out-of-plane direction in BCN and BCP than in-plane motion of atoms as flexural mode has comparatively small frequency than transverse and longitudinal acoustic modes.

3.2. Electronic structure

The calculated band structure of BCN and BCP are shown in Fig. 3. From the band structure, it is seen that BCN exhibit an indirect bandgap with valence band maximum (VBM) located at Γ -point and conduction band minimum (CBM) occurs at point-X. On the other hand, BCP is found to have direct bandgap which occurs between Γ - and X-point of the Brillouin zone. The calculated bandgap of BCN and BCP were 1.97 eV and 0.552 eV, respectively. It is clear from Fig. 3 that both BCN and BCP exhibit substantial dispersion in the band structures. Both

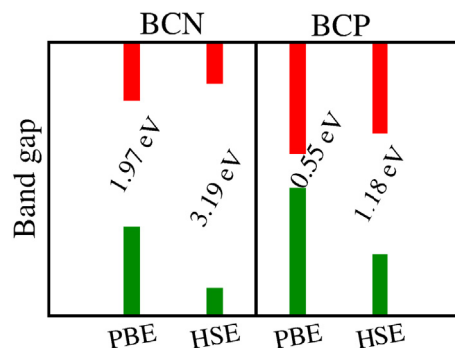


Fig. 2. Band gap of BCN and BCP from PBE and HSE functional, respectively.

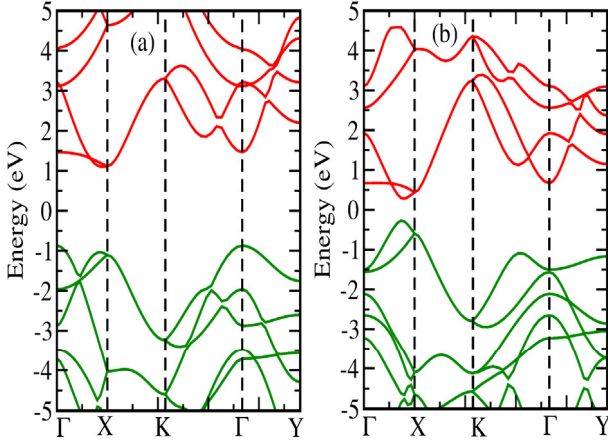


Fig. 3. The calculated band structures of (a) BCN and (b) BCP.

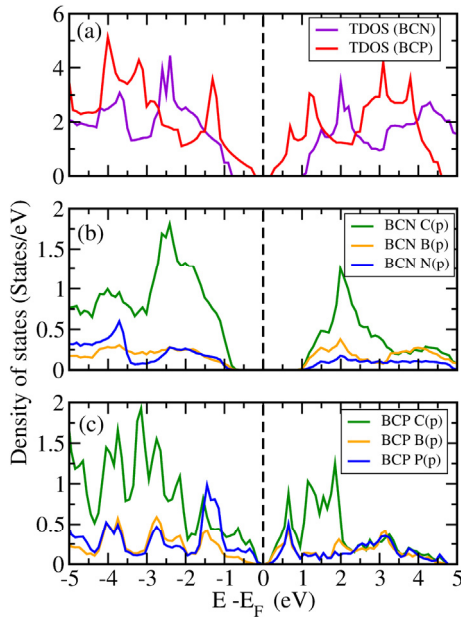


Fig. 4. Total density of states of (a) BCN and BCP, partial density of states of (b) BCN and (c) BCP.

structures show parabolic nature of CBM and VBM which implies that deformation potential theory can be applied for such systems. Moreover, as it is well-known fact that DFT with PBE functional always underestimates the bandgap [37,38]. Therefore, we employed the HSE functional to accurately determine the bandgap. The calculated bandgap values of BCN and BCP were 3.19 eV and 1.18 eV as depicted in Fig. 2. From HSE results, one can predict that BCN is a wide bandgap semiconductor. It is well known that Silicon which has revolutionized the micro-electronic industry exhibit an indirect bandgap (1.21 eV). Herein, we showed that BCP is an interesting material that shows a direct bandgap (1.18 eV) which is very close to that of Silicon. These results indicates that BCP is an exciting material for future nano- and opto-electronic devices. We also examined the total and partial density of states (PDOS) of BCN and BCP, which are shown in Fig. 4. From the total density of states, it is apparent that BCN shows larger bandgap than BCP. From PDOS of BCN, it is observed that both CBM and VBM are dominated by Carbon p-orbital where as in BCP, CBM and VBM possess nearly equal contribution from boron, Carbon and phosphorus.

4. Carrier mobility

The carrier mobility is a dominant feature to assess the electrical performance of materials. Carrier mobility depends on the effective mass, which in turn is affected by strain. The carrier mobility in 2D materials at room temperature is dominated by acoustic phonon scattering via intra- and inter-valley deformation potential (DP) couplings at room temperature [39,40]. Bardeen and Shockley reported that deformation potential theory can be used to calculate the carrier mobility [41]. Using effective mass approximation and DP theory, the mobility of 2D materials can be determined as [42,43]

$$\mu_{2D} = \frac{e\hbar^3 C_{2D}}{k_B T m^{*2} (E^i)^2} \quad (2)$$

where m^* is the effective mass of charge carriers in the transport direction, E^i represents the deformation potential constant of the conduction band minimum (CBM) for electrons or valence band maximum (VBM) for holes along the transport direction which is defined by $E^i = \Delta V_i / \epsilon$. Here ΔE_i is the energy change of the i th band under cell compression or dilatation, ϵ is the applied strain that is defined as $\epsilon = \Delta l / l_0$, where l_0 is the equilibrium lattice constant in the transport direction and Δl_0 is the deformation of l_0 . The elastic modulus C_{2D} of the longitudinal strain in the propagation directions (both x and y) of the longitudinal acoustic wave is calculated from parabolic fitting of the equation $(E - E_0) / S_0 = C_{2D} \epsilon^2 / 2$, where E denotes the total energy of deformed system, E_0 is the energy of system in equilibrium, and S_0 is the area of a system at equilibrium. The temperature used for mobility calculation is 300 K for each case.

The effective mass strongly influence the carrier mobility of a material, which in the present case was calculated by parabolic fitting the E versus k curve ($m^{*-1} = \frac{1}{\hbar^2} \frac{\partial^2 E}{\partial k^2}$) for holes and electrons in the vicinity of VBM and CBM, respectively. Apart from effective mass, phonon scattering also limit the carrier mobility and this effect is depicted in elastic constant and deformation potential constant. All these parameters were calculated using PBE functional. Figs. SI.1 and SI.2 present the plots of total energy and ΔE_i versus uniaxial strain, which is varied from -2% to 2% . It is apparent from Figs. SI.1 and SI.2 that an excellent fitting has been observed in both cases. The carrier mobility and other related parameters obtained for BCX ($X = N, P$) are shown in Table 1. From the table, it is obvious that effective mass and mobility of both electron and hole show anisotropic behavior. The elastic modulus of both systems were also found to exhibit anisotropic nature. For BCN, it is seen that electron has higher mobility ($\mu_x^e = 2.0\mu_y^e$) along x-direction as compared to the mobility along y-direction, whereas hole shows larger mobility ($\mu_y^h = 7.13\mu_x^h$) in y-direction. In case of BCP, it is observed that mobility of electron is ($\mu_x^e = 1.25\mu_y^e$) more along x-direction while the hole shows larger mobility along ($\mu_x^h = 1.97\mu_y^h$) along x. Also, among the two systems, it is revealed that BCP exhibit large carrier mobility for both electrons and holes compared to BCN. This may be due to the fact that BCN exhibit larger bandgap than BCP. The mobility of electrons and holes in Silicon is $1400 \text{ cm}^2 \text{V}^{-1} \text{s}^{-1}$ [7] Graphene itself was reported to

Table 1

The calculated effective mass, deformation potential (eV), elastic modulus (Jm^{-2}), and charge mobility ($\mu \text{ cm}^2 \text{V}^{-1} \text{s}^{-1}$) of monolayer BCX ($X = N, P$).

	carrier type	axis	m/m_0	E_i	C_{2D}	μ
BCN	e	x	1.222	-4.722	275.141	176
		y	1.610	-5.288	298.500	88
	h	x	0.947	-16.705	275.141	23
		y	1.247	4.910	298.500	164
BCP	e	x	0.489	-3.354	204.203	1588
		y	0.435	-1.878	200.660	2990
	h	x	0.636	-3.788	204.203	1607
		y	0.561	-4.031	200.660	838

m_0 is the rest mass of electron.

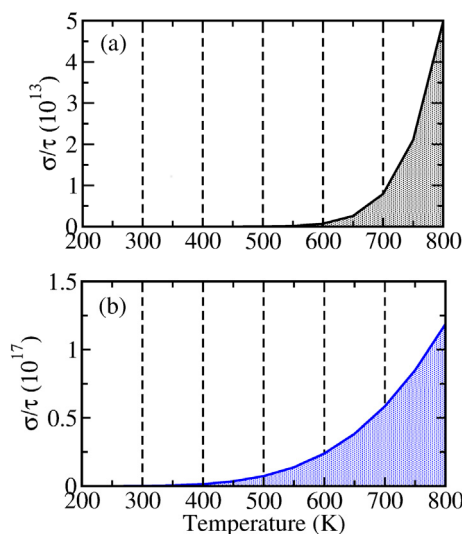


Fig. 5. Conductivity in units of ($\Omega^{-1}\text{cm}^{-1}\text{s}^{-1}$) as a function of temperature, (a) BCN and (b) BCP.

have ultrahigh carrier mobility of $1\text{--}4 \times 10^5 \text{cm}^2\text{V}^{-1}\text{s}^{-1}$ [8], however, semi-metallic band structure of graphene restricts its wide application in because of the low ON/OFF current ratio [44]. Transition metal dichalcogenides such as MoS_2 and WSe_2 , show suitable ON/OFF ratios but their carrier mobility values are low, $\approx 100 \text{cm}^2\text{V}^{-1}\text{s}^{-1}$ [7]. The calculated mobility of BCP in the present study is $2990 \text{cm}^2\text{V}^{-1}\text{s}^{-1}$ for electrons and $1607 \text{cm}^2\text{V}^{-1}\text{s}^{-1}$ for holes. This shows that carrier mobility of BCP is significantly larger than Silicon and transition metal dichalcogenides.

Further, the conductivity of BCN and BCP were also determined by means of the semiclassical Boltzmann theory within constant relaxation time approximation using BoltzTrap code [45,46]. In this approach, the conductivity is calculated using the equation

$$\sigma_{\alpha,\beta}(T, \nu) = \sum_i \int \frac{dk}{8\pi} \left[-\frac{\partial f(T, \nu)}{\partial \epsilon} \right] \sigma_{\alpha,\beta}(i, k) \quad (3)$$

where f is the Fermi-Dirac distribution function and ν is the chemical potential that is determined by the number of free carriers. Here, $\sigma_{\alpha,\beta}(i, k) = e^2 v_{i,k} v_{\alpha}(i, k) v_{\beta}(i, k)$ is the conductivity tensor in which $v(i, k) = \hbar^{-1} \frac{\partial \epsilon_{i,k}}{\partial k_{\alpha}}$ represents the group velocity of i th band for α component. The calculated conductivity (σ/τ) using BoltzTrap code is shown in Fig. 5. From the figure, it is apparent that conductivity of BCP increase with temperature much earlier as compared to BCN. The conductivity of BCP at 300 K was found to be 1.203×10^{14} whereas BCN has nearly zero conductivity at room temperature. The reason for finite conductivity in BCP at room temperature may be due to small direct bandgap (1.18 eV) in BCP compared to BCN which has an indirect bandgap of 3.19 eV.

5. Conclusions

We performed DFT calculations to investigate the structural, electronic, phonon and carrier transport properties of BCN and BCP. From phonon dispersion results, it is predicted that both BCN and BCP are dynamically stable structures. Cohesive energy values reveal that BCN is relatively more stable than BCP. The calculated PBE band structure shows that BCN is an indirect bandgap (1.97 eV) semiconductor whereas BCP displays a direct bandgap (0.55 eV). Bandgaps values calculated using HSE functional shows BCN is a wide bandgap (3.19 eV) semiconductor whereas the bandgap of BCP (1.18 eV) was found to be comparable to silicon. Considering the carrier mobility of electrons and holes, it is observed that in both materials, electron mobility dominates to that of holes. Electron/hole mobility of BCP was found on the order

of $10^3 \text{cm}^2\text{V}^{-1}\text{s}^{-1}$ that is significantly larger than MoS_2 and Silicon, which shows that BCP is an attractive material for future electronic applications. We conclude that by rationally co-doping graphene with boron and phosphorus may result in new materials with appealing electronic properties.

Author contributions

VKY and SHM performed all calculations and contributed equally in preparing the manuscript. VKY, SHM and JKS analyze the results and wrote the manuscript.

Acknowledgment

VKY acknowledge the funding from Department of Science and Technology (grant no. SB/S3/CE/079/2015 and DST/TM/WTI/2K15/112(G)). SHM gratefully acknowledge the Institute Postdoctoral fellowship (IPDF) from Department of Chemistry at IIT Kanpur. The authors are thankful to the HPC centre IIT Kanpur for providing computational facility.

Appendix A. Supplementary data

Supplementary data to this article can be found online at <https://doi.org/10.1016/j.physb.2019.07.017>.

References

- [1] M. Zheng, I. Ghosh, B. Konig, X. Wang, *ChemCatChem* 11 (2019) 703–706.
- [2] G.F. Moore, I.D. Sharp, *J. Phys. Chem. Lett.* 4 (2013) 568–572.
- [3] H. Fei, R. Ye, G. Ye, Y. Gong, Z. Peng, X. Fan, E.L.G. Samuel, P.M. Ajayan, J.M. Tour, *ACS Nano* 8 (2014) 10837–10843.
- [4] C. Yu, Z. Liu, X. Meng, B. Lu, D. Cui, J. Qiu, *Nanoscale* 8 (2016) 17458.
- [5] J. Zhang, L. Dai, *Angew. Chem. Int. Ed.* 55 (2016) 13296–13300.
- [6] K.S. Novoselov, A.K. Geim, S.V. Morozov, D. Jiang, M. I. Katsnelson, I.V. Grigorieva, S.V. Dubonos, A.A. Firsov, *Nature* 438 (2005) 197.
- [7] F. Ruhao, X. Cui, M.A. Khan, C. Stampfl, S.P. Ringer, Rongkun Zheng, *Adv. Electron. Mater.* (2019) 1800797.
- [8] *Solid State Commun.* 146 (2008) 351.
- [9] S. Ullah, P.A. Denis, F. Sato, *ChemPhysChem* 18 (2017) 1864–1873.
- [10] M. Chhetri, S. Maitra, H. Chakraborty, U.V. Waghmare, C.N.R. Rao, *Energy Environ. Sci.* 9 (2017) 95–101.
- [11] S. Banerjee, G. Periyasamy, S.K. Pati, *J. Mater. Chem. A* 2 (11) (2014) 3856–3864.
- [12] S. Banerjee, S. Neihisal, S.K. Pati, *J. Mater. Chem. A* 4 (15) (2016) 5517–5527.
- [13] S. Banerjee, S.K. Pati, *Nanoscale* 6 (22) (2014) 13430–13434.
- [14] S. Yu, H.D. Xiong, K. Eshun, H. Yuan, Q. Li, *Appl. Surf. Sci.* 325 (2015) 27–32.
- [15] S. Mukherjee, T.P. Kaloni, *J. Nanoparticle Res.* 14 (2012) 1059.
- [16] L. Wang, Z. Sofer, P. Simek, I. Tomandl, M. Pumera, *J. Phys. Chem. C* 117 (2013) 23251–23257.
- [17] N. Al-Aqtash, I. Vasiliev, *J. Phys. Chem. C* 115 (2011) 18500–18510.
- [18] A. Laref, A. Ahmed, S. Binomran, S.J. Luo, *Carbon* 81 (2015) 179–192.
- [19] Z. Wang, P. Li, Y. Chen, J. He, W. Zhang, O.G. Schmidt, Y. Li, *Nanoscale* 6 (2014) 687–694.
- [20] H.L. Poh, P. Simek, Z. Sofer, M. Pumera, *ACS Nano* 7 (2013) 5262–5272.
- [21] F. Niu, L.-M. Tao, Y.-C. Deng, Q.-H. Wang, W.-G. Song, *New J. Chem.* 30 (2014) 2269–2272.
- [22] C. Bronner, S. Stremmlau, M. Gille, F. Brausse, A. Haase, S. Hecht, P. Tegeder, *Angew. Chem. Int. Ed.* 52 (2013) 4422–4425.
- [23] S. Kawai, S. Saito, S. Osumi, S. Yamaguchi, A.S. Foster, P. Spijker, E. Meyer, *Nat. Commun.* 6 (2015) 8098.
- [24] H.S. Kim, S.S. Kim, H.S. Kim, Y.-H. Kim, *Nanotechnology* 27 (6pp) (2016) 47LT01.
- [25] E. Cruz-Silva, F. Lopez-Urias, E. Munoz-Sandoval, B.G. Sumpter, H. Terrones, J.C. Charlie, V. Meunier, M. Terrones, *ACS Nano* 3 (2009) 1913–1921.
- [26] H.S. Kim, H.S. Kim, S.S. Kim, Y.H. Kim, *Nanoscale* 6 (2014) 14911–14918.
- [27] V.K. Yadav, S.H. Mir, J.K. Singh, *ChemPhysChem* 20 (2019) 1–9.
- [28] S.H. Mir, V.K. Yadav, J.K. Singh, *ACS Omega* 4 (2019) 3732–3738.
- [29] P. Giannozzi, S. Baroni, N. Bonini, M. Calandra, R. Car, C. Cavazzoni, D. Ceresoli, G.L. Chiarotti, M. Cococcioni, I. Dabo, et al., *J. Phys. Condens. Matter* 21 (39) (2009) 395502.
- [30] J.P. Perdew, K. Burke, M. Ernzerhof, *Phys. Rev. Lett.* 77 (18) (1996) 3865.
- [31] J.P. Perdew, J.A. Chevary, S.H. Vosko, K.A. Jackson, M.R. Pederson, D.J. Singh, C. Fiolhais, *Phys. Rev. B* 46 (1992) 6671.
- [32] H.J. Monkhorst, J.P. Pack, *Phys. Rev. B* 13 (1976) 5188.
- [33] S. Grimme, J. Antony, S. Ehrlich, H. Krieg, *J. Chem. Phys.* 132 (2010) 154104.
- [34] J. Heyd, G.E. Scuseria, M. Ernzerhof, *J. Chem. Phys.* 118 (2003) 8207–8215.
- [35] S.H. Mir, P.C. Jha, S. Dabhi, P.K. Jha, *Mater. Chem. Phys.* 175 (2016) 54–61.
- [36] L.A. Falkovsky, *Phys. Lett. A* 372 (2008) 5189–5192.

- [37] J.P. Perdew, *Int. J. Quantum Chem.* 28 (1985) 497–523.
- [38] A. Pribram-Jones, D.A. Gross, K. Burke, *Annu. Rev. Phys. Chem.* 66 (2015) 283–304.
- [39] K. Kaasbjerg, K.S. Thygesen, K.W. Jacobsen, *Phys. Rev. B* 85 (11) (2012) 115317.
- [40] K. Kaasbjerg, K.S. Thygesen, A.P. Jauho, *Phys. Rev. B* 87 (23) (2013) 235312.
- [41] J. Bardeen, W. Shockley, *Phys. Rev.* 80 (1) (1950) 72.
- [42] R. Fang, C. Xiangyuan, A.K. Mansoor, S. Catherine, S.P. Ringer, R. Zheng, *Adv. Electron. Mater.* (2019), <https://doi.org/10.1002/aelm.201800797>.
- [43] S. Bruzzone, G. Fiori, *Appl. Phys. Lett.* 99 (2011) 222108.
- [44] I. Meric, M.Y. Han, A.F. Young, B. Ozyilmaz, P. Kim, K.L. Shepard, *Nat. Nanotechnol.* 3 (2008) 654.
- [45] C. Motta, F. El-Mellouhi, S. Sanvito, *Sci. Rep.* 5 (2015) 12746.
- [46] G. Madsen, D. Singh, *Comput. Phys. Commun.* 175 (2006) 6771.